

T-ray tomography

Daniel M. Mittleman,* Stefan Hunsche, Luc Boivin, and Martin C. Nuss

Bell Laboratories, Lucent Technologies, 101 Crawfords Corner Road, Holmdel, New Jersey 07733

Received March 24, 1997

We demonstrate tomographic T-ray imaging, using the timing information present in terahertz (THz) pulses in a reflection geometry. THz pulses are reflected from refractive-index discontinuities inside an object, and the time delays of these pulses are used to determine the positions of the discontinuities along the propagation direction. In this fashion a tomographic image can be constructed. © 1997 Optical Society of America

We recently described a new imaging modality, based on time-resolved measurements of picosecond bursts of electromagnetic radiation in the terahertz (THz) frequency range.¹ Although THz time-domain measurements have been used successfully for spectroscopy,^{2,3} imaging with THz pulses has not been practical owing to the long (minutes) acquisition times for the THz waveforms. Our new T-ray imaging technique is made possible by reduction of the acquisition time of a single THz waveform from several minutes to several milliseconds, while a signal–noise ratio of >1000:1 is maintained.⁴ In the original demonstration,¹ no explicit use of the time-domain nature of the THz pulses was made, and the images displayed only the transmitted power obtained by integration of the Fourier spectrum of the THz waveform with a digital signal processor. There is much more spectroscopic information available from the THz waveforms, such as timing, broadening, and other temporal distortions that result from the frequency-dependent absorption and dispersion of the object. These temporal distortions can be analyzed in real time to yield compositional information about the sample. For example, we recently demonstrated real-time recognition of gases and gas mixtures, using linear predictive coding as a waveform classification and recognition procedure.⁵

In this Letter we report on the extension of T-ray imaging to three-dimensional tomographic imaging by analyzing the temporal structure of THz waveforms returned from objects in a reflection geometry. The return time of reflected pulses directly correlates with the location of the dielectric interfaces along the propagation direction of the beam. Because the arrival time of the THz waveforms can be determined with an accuracy of a few femtoseconds, i.e., much less than the pulse duration, the positions of reflecting surfaces within the object under study can be determined with an accuracy of a few micrometers when successive reflections are well separated in time.⁴ In contrast with the two-dimensional T-ray transmission images published earlier,¹ full volume images of many objects in the THz frequency range can now be obtained.

The experimental setup is described in detail in Ref. 4. The beam of THz pulses is incident upon the sample at nearly normal incidence and comes to a focus at the sample surface. The beam reflected from the object is recollimated and then captured by a pick-off mirror, which directs it to the receiver antenna. The generation, detection, and real-time processing of the

THz waveforms are similar to what is described in the original transmission experiments.^{1,4} For an object with multiple reflecting internal surfaces, the reflected waveform consists of a series of replicas of the input pulse of varying magnitude, polarity, and temporal distortion. We illustrate this, using the example of a 3.5-in. floppy disk, with the input and reflected THz waveforms from a single point on the floppy disk shown in Fig. 1. We obtain waveform (a) by replacing the object with a mirror, and thus the pulse that is incident upon the sample is represented. The small oscillations that follow the main pulse in this waveform are a result of residual water vapor in the beam path⁶ and do not affect the measurement significantly. Curve (b), a representative reflected waveform, consists of a

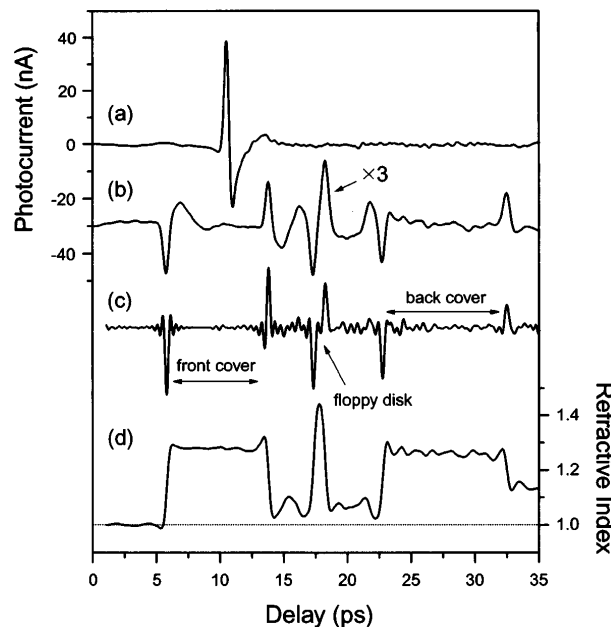


Fig. 1. (a) Input THz waveform and (b) reflected waveform from a single point on a 3.5-in. floppy disk. Each of the reflected pulses identifies a dielectric discontinuity along the propagation direction of the beam normal to the floppy disk, as labeled in the figure. Curve (c) is the reflected waveform after signal processing, as described in the text. Curve (d) is the refractive-index profile of the medium (right-hand axis), derived from curve (c) by Eqs. (3) and (4) below. Curve (b) has been scaled up by a factor of 3 relative to the left (photocurrent) axis and vertically offset for clarity.

series of replicas of the input waveform. These correspond to reflections from the dielectric interfaces of the floppy disk from air to plastic, from plastic to air, or from surfaces of the magnetic recording material. The polarity and the magnitude of each reflection are given by the reflection coefficient at each interface and are related to the size and sign of the corresponding index step. The four reflections resulting from the front and back plastic covers are clearly resolved. However, the thickness of the magnetic recording material is so small that the waveforms returned from its front and back surfaces cannot be distinguished and appear as a single distorted waveform. In this example the temporal waveforms hardly change shape while traversing the object because the plastic material has little absorption and dispersion. In a more general situation, reflected waveforms may be significantly altered in shape.

In Fig. 1, (c) is the waveform of (b) after numerical Fourier deconvolution (i.e., division of the Fourier spectra of the incident and the reflected waveforms, with a low-pass filter to remove noise above ~ 2.5 THz). Subsequently, low-frequency background is removed by means of wavelet filtering.⁷ This procedure produces a sharp spike at a time delay corresponding to the position of every reflecting interface. Thus it helps to determine more accurately the positions of the various interfaces. In contrast with (b) in Fig. 1, the front and back surfaces of the thin ($\sim 120\text{-}\mu\text{m}$) magnetic recording material are clearly resolved in the deconvolved data (c). This is consistent with the expected resolution of $L_c/2$, where $L_c = 200\text{ }\mu\text{m}$ is the coherence length of the THz pulse in the intervening material. In contrast, when no other reflections are nearby, we find that the position of a reflecting surface can be determined with a precision of only a few micrometers.⁴

Figure 2 shows a conventional T-ray image of a section of the floppy disk obtained in reflection [Fig. 2(a)] and a tomographic slice [Fig. 2(b)] at a fixed vertical position. We obtained the conventional T-ray image at the top by computing the total reflected power, using real-time processing of the reflected waveforms with a digital signal processor,^{1,4} with the reflected power translated into a gray scale. The plastic cover with its various features, the circular recording disk, and the metallic hub in the center of the disk can be distinguished.

In Fig. 2(b) a tomographic T-ray slice of the floppy disk is shown at a particular vertical position ($y = 15\text{ mm}$), indicated by the dashed line in Fig. 2(a). For each horizontal (x) position a reflected waveform is acquired, processed as described above [curve (c), Fig. 1], and displayed as a function of delay in this tomographic image. The amplitude of the processed waveforms is translated into a gray scale so that each reflecting surface appears as a stripe. The positions of the various parts of the floppy disk along the propagation direction of the THz beam, such as the front and back covers, the magnetic recording disk, and the metal hub, can be observed clearly in this tomographic picture. The image also shows some artifacts of the technique that result from multiple

reflections among the various interfaces, such as the features observed behind the (opaque) metal hub, as well as the apparent discontinuity in the magnetic recording medium caused by a change in the thickness of the front plastic cover at $x = 12\text{ mm}$.

Signal processing of the THz waveforms can be used to extract the layer structure of the medium at any given (x, y) position. The reflected waveform $B(t)$ is related to the input waveform $A(t)$ by a convolution with the impulse response $g(t)$ of the layered medium:

$$B_j = \sum_{k=0}^M g_{j-k} A_k . \quad (1)$$

In Eq. (1) discrete-time functions defined by digitization with a time step Δt [e.g., $B_k = B(k\Delta t)$] are used. M is the number of samples in the digitized waveforms, 1024 in these examples. The impulse response $g(t)$ is characteristic of the object and does not depend on the details of the input pulse. The coefficients g_k are determined by the reflection off the k th layer as well as by the transmission through the preceding layers, $j = 1, \dots, k - 1$, once in each direction. The distance d_j between two adjacent layers j and $j + 1$ is related to the time separation of the two corresponding reflections $\Delta t = t_{j+1} - t_j$ by

$$d_j = \frac{c}{2n_j} \Delta t , \quad (2)$$

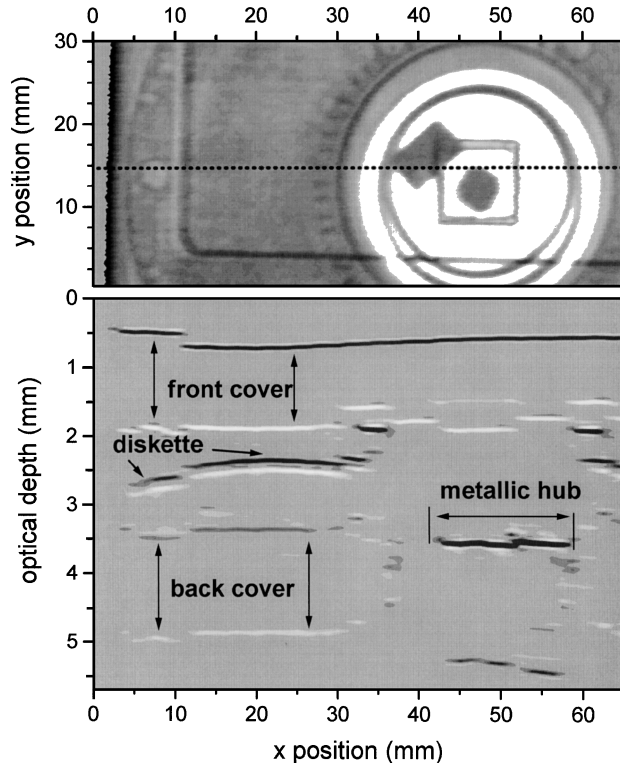


Fig. 2. (a) Conventional reflective T-ray image of the 3.5-in. floppy disk and (b) tomographic image of the same disk at a constant vertical position, indicated by the dashed line at $y = 15\text{ mm}$ in (a). Darker stripes indicate positive refractive-index steps ($\Delta n > 0$), and lighter stripes indicate negative steps ($\Delta n < 0$). The vertical axis (optical delay) is related to the waveform delay by Eq. (2), neglecting all refractive-index variations.

where n_j is the refractive index of the medium between surfaces j and $j + 1$. Therefore the temporal position of each reflected pulse is related to the depth of the reflecting interface.

An approximation for the impulse response function is obtained from a numerical deconvolution of the measured waveforms $A(t)$ and $B(t)$, such as those shown in Fig. 1, curve (c). Given $g(t)$, one can reconstruct the refractive-index profile of the layered structure. In discretized form, the j th time step corresponds to a layer of thickness d_j given by Eq. (2) and of refractive index n_j given by

$$n_j = \prod_{i=1}^j \frac{1 - r_i}{1 + r_i}, \quad (3)$$

where the reflection coefficients r_k are defined iteratively by

$$r_k = g_k \prod_{j=1}^{k-1} \frac{1}{(1 - r_j)^2}. \quad (4)$$

Here $r_1 = g_1$, and, by definition, the initial reference plane has $n_0 = 1$.

These expressions are valid in the limit of small reflection coefficients when multiple reflections are negligible. Also, absorption and dispersion effects are neglected. Finally, the finite widths of the features in Fig. 1, curve (c) (resulting from the finite bandwidth of the source) are not accounted for in Eqs. (3) and (4).

Equations (3) and (4) can be used as a basis for an algorithm to derive the refractive-index profile of the medium, given the impulse response function. In the present example Eqs. (3) and (4) were used to derive the index profile of the floppy disk from the experimental impulse response function shown in Fig. 1, curve (c). The result is shown in curve (d) of Fig. 1. There the profile is fairly well reproduced, although the index does not return completely to $n = 1$ in the free-space regions. This is because of the aforementioned simplifications, most particularly the effect of the finite source bandwidth, which spreads the index discontinuity over a finite length. A more sophisticated algorithm for calculating the index profile would include the finite bandwidth of the THz source explicitly as well as the frequency-dependent complex index of the material. Then one could use Eq. (2) to calibrate the depth axis in a tomographic image. This would eliminate artifacts such as the apparent discontinuities in continuous surfaces mentioned above.

It is worth noting that a full three-dimensional representation of the object can be built just as rapidly as a two-dimensional image, because all the information about the third dimension (the depth) is contained in a single waveform. For example, the image in Fig. 2(b) consists of 217 waveforms and took <11 s to acquire.

Tomographic T-ray imaging is similar in principle to ultrasonic imaging.⁸ A commonly encountered problem in ultrasonic imaging is the large difference in acoustic impedance between air and liquid or solid objects, which necessitates some form of index matching. For THz waves, the dielectric constants

of many materials are not too different from that of air, and index matching therefore is not required. Many materials such as plastics, cardboard, wood, and rubber have good transparency in the THz frequency range. Hence, this new technology can be effectively used in many quality-control applications, for example, to detect voids or cracks. Another application area for T-ray tomography is burn diagnostics. Although strong water absorption precludes the use of THz radiation in biomedical research inside the body, it may be possible to obtain quantitative and highly sensitive measurements of burn depth and burned tissue properties by use of THz tomography in dermatological medicine.⁴

In conclusion, the recent research on imaging with THz waves has been expanded here to include imaging in a reflection geometry. Here timing information is correlated with depth information, and we have found that tomographic slices of objects can be obtained, with the possibility of three-dimensional T-ray tomography on a wide range of samples. In T-ray tomographic imaging one can isolate in the time domain successive reflections and extract information about each layer of a layered material individually. In this fashion detailed spectroscopic information about subsurface layers can be obtained, with the potential for material identification. The range of potential applications for T-ray tomography is extremely broad, encompassing such wide-ranging fields as biomedical imaging, package inspection, and quality control.

S. Hunsche acknowledges the support of the Alexander von Humboldt Foundation.

*Present address, Department of Electrical and Computer Engineering, Rice University, MS-366, 6100 Main Street, Houston, Texas 77005. E-mail: daniel@rice.edu.

References

1. B. B. Hu and M. C. Nuss, Opt. Lett. **20**, 1716 (1995).
2. D. Grischkowsky, S. Keiding, M. van Exter, and C. Fattinger, J. Opt. Soc. Am. B **7**, 2006 (1990); N. Katzenellenbogen and D. Grischkowsky, Appl. Phys. Lett. **61**, 840 (1992).
3. M. C. Nuss and J. Orenstein, in *Millimeter-Wave Spectroscopy of Solids*, G. Gruener, ed. (Springer-Verlag, Berlin, 1997).
4. D. M. Mittleman, R. H. Jacobsen, and M. C. Nuss, IEEE J. Sel. Topics Quantum Electron. **2**, 679 (1997).
5. R. H. Jacobsen, D. M. Mittleman, and M. C. Nuss, Opt. Lett. **21**, 2011 (1996).
6. M. van Exter, C. Fattinger, and D. Grischkowsky, Opt. Lett. **14**, 1128 (1989).
7. Wavelet processing was performed with the WaveLab software package of J. Buckheit, S. Chen, D. Donoho, I. Johnstone, and J. Scargle, of the Department of Statistics at Stanford University, available on the World Wide Web at <http://playfair.stanford.edu/~wavelab/>.
8. A. C. Kak and M. Slaney, *Principles of Computerized Tomographic Imaging* (IEEE Press, New York, 1988).